

Desorption Behaviours of Lithium Alanate with Metal Oxide Nanopowder Additives

M. Ismail^{1,*}, A. M. Sinin², C. K. Sheng³, W. B. Wan Nik¹

¹School of Ocean Engineering, Universiti Malaysia Terengganu, 21030 Kuala Terengganu, Malaysia

²School of Fundamental Education and Liberal, Universiti Malaysia Terengganu, 21030 Kuala Terengganu, Malaysia

³School of Fundamental Science, Universiti Malaysia Terengganu, 21030 Kuala Terengganu, Malaysia

*E-mail: mohammadismail@umt.edu.my

Received: 21 April 2014 / Accepted: 27 May 2014 / Published: 16 June 2014

The effects of metal oxide nanopowder (Fe_2O_3 , Cr_2O_3 , ZnO and MoO_3) additions by dry ball milling on the hydrogen desorption behaviours of LiAlH_4 have been investigated. Among them, adding Fe_2O_3 leads to the most pronounced improvement on the onset dehydrogenation temperature and desorption kinetic rate. The dehydrogenation temperature of the 5 wt.% Fe_2O_3 -doped LiAlH_4 sample was reduced to 80 °C and 145 °C in the first and second stages, respectively, compared with 150 °C and 180 °C for the as-received LiAlH_4 . In terms of the desorption kinetics, the 5 wt.% Fe_2O_3 -doped LiAlH_4 sample released about 3.8 wt.% hydrogen at 90 °C after 60 minutes of dehydrogenation, but all the other doped samples released less than 0.7 wt.% hydrogen under the same conditions. From the Kissinger plot based on differential scanning calorimetry at different heating rates, the apparent activation energy of the as-received LiAlH_4 was calculated to be 102 and 110 kJ/mol for the first two dehydrogenation steps, and these values were reduced by 84 and 96 kJ/mol, respectively, after being doped with Fe_2O_3 . Based on the X-ray diffraction and Fourier transform infrared spectroscopy examinations, it is believed that the significant improvement of LiAlH_4 dehydrogenation properties in the Fe_2O_3 -doped samples was due to the synergetically catalytic effects of the in-situ generated Li_5FeO_4 and $\text{Fe}_{0.974}\text{O}$ that were formed during the milling process.

Keywords: Hydrogen storage; complex hydride; lithium alanate; metal oxide; dehydrogenation properties

1. INTRODUCTION

Due to the environmental crisis and the limited supply of fossil fuels, hydrogen has attracted much attention as an alternative energy carrier [1]. However, hydrogen storage is a significant challenge for the development of a hydrogen economy, especially for hydrogen-powered vehicles.

There are three methods to store hydrogen, namely, high pressure, cryogenics, and solid-state storage. Among them, solid-state storage has become an attractive option due to its high volumetric hydrogen capacity and favourable safety considerations. However, until now, no single material can satisfy all the requirements for an on-board hydrogen storage material suitable for mobile applications due to drawbacks in the de/rehydrogenation kinetics or thermodynamics.

Solid-state hydrogen storage can be divided into two main categories. The first category is physically bound hydrogen, where the hydrogen gas is physisorbed to a high surface area substrate (exterior or interior) such as carbon nanotubes [2,3]. The second category is chemically bound hydrogen, where the hydrogen has formed a chemical compound with the substrate (e.g., metal hydrides [4-10] and complex hydrides [11-16]) and the hydrogen is desorbed through a thermal decomposition. Before 1997, complex hydride did not attract much attention as a hydrogen storage medium until the discovery by Bogdanovic and Schwickardi [17]. Their study showed that doping NaAlH₄ with Ti compounds enabled reversibility of the hydrogenation/dehydrogenation reaction. Since then, extensive catalyst investigations have been reported for the development of solid-state hydrogen storage, especially in light metal hydrides, including LiAlH₄. LiAlH₄ theoretically contains 7.9 wt.% H₂, making it a preferable hydrogen storage medium to NaAlH₄ in terms of gravimetric capacity for hydrogen vehicles. LiAlH₄ theoretically can release about 7.9 wt.% of hydrogen in two stages according to the following reactions [18]:



The first reaction stage releases 5.3 wt.% H₂ and requires 150-175 °C and the second reaction stage releases 2.6 wt.% H₂ and requires 180-220 °C.

Although LiAlH₄ possesses higher hydrogen storage capacity compared to NaAlH₄, the high onset decomposition temperature and slow desorption kinetics constrain its practical applications. Many studies have been conducted to overcome these problems by adding different kinds of catalysts. Among them, metal oxides have been successfully used to improve the dehydrogenation properties of LiAlH₄. However, the studies of metal oxides as a catalyst for LiAlH₄ have not been reported as thoroughly as other catalysts such as pure metal [19-26], metal halides [19,27-38], and carbon-based catalysts [39-43]. Until now, to the best of the author's knowledge, only a few kinds of metal oxides (TiO₂ [37,38,44], Cr₂O₃ [45], Nb₂O₃ [45], MnFe₂O₄ [46], Fe₂O₃ [47], Co₂O₃ [47], CeO₂[48], NiCo₂O₄ [49], NiFe₂O₄ [50], and CoFe₂O₄ [51]) have been used as catalysts for LiAlH₄. Therefore, it is desirable to explore the effect of other metal oxide-based additives on the dehydrogenation behaviours of LiAlH₄.

It is believed that the newly formed ball-milled or dehydrogenation product in the LiAlH₄ catalyst system could act as a real catalyst to facilitate the dehydrogenation steps of LiAlH₄ [46]. These products could create surface activation and form a large amount of nucleation sites at the surface of the LiAlH₄ matrix. It is also believed that the finely dispersed dehydrogenated products may contribute to kinetic desorption improvement by serving as the active sites for nucleation and creation of the dehydrogenation product by shortening the diffusion distance of the reaction ions [46].

Focusing on the role of ball-milled or dehydrogenation products in the improvement of the dehydrogenation LiAlH₄, in this study, a series of metal oxide nanopowder (Fe₂O₃, Cr₂O₃, ZnO and

MoO₃) were used as catalyst for LiAlH₄. Samples were analysed by a Sievert-type pressure-composition-temperature (PCT) apparatus, differential scanning calorimetry (DSC), X-ray diffraction (XRD), and Fourier transform infrared (FTIR) spectroscopy.

2. EXPERIMENTAL PROCEDURES

LiAlH₄ (powder, reagent grade, 95% purity), Fe₂O₃ (nanopowder, <50 nm particle size (BET)), Cr₂O₃ (nanopowder, <100 nm particle size (TEM), 99% trace metals basis), MoO₃ (nanopowder, 100 nm (TEM), 99.5% trace metals basis) and ZnO (nanopowder, <100 nm particle size) were purchased from Sigma-Aldrich and were used as received with no further purification. Approximately 2 g of LiAlH₄ was mixed with 5 wt.% of metal oxides and the mixture was loaded into a sealed stainless steel vial together with hardened stainless steel balls in an argon atmosphere MBraun UNILab glove box. The ratio of the weight of balls to the weight of powder was 40:1. The sample was then milled in a planetary ball mill (NQM-0.4) for 1 hour, by first milling for 0.5 hours, resting for 6 minutes, and then milling for another 0.5 hours in a different direction at the rate of 400 rpm. Pure LiAlH₄ was also prepared under the same conditions for comparison purposes.

The measurements for dehydrogenation and rehydrogenation were performed in a Sievert-type PCT apparatus (Advanced Materials Corporation). About 200 mg of the sample was loaded into a sample vessel. This apparatus can operate at up to 200 atm and 900 °C. For desorption purposes, all the samples were heated under a controlled vacuum of 0.1 atm. The heating rate for the desorption experiment was 5 °C/min, and the samples were heated from room temperature to the desired temperature under a vacuum. Rehydrogenation studies were carried out with LiAlH₄ doped with 5 wt.% Fe₂O₃. After the first complete dehydrogenation (the first two stages of reaction), the samples were kept at different temperatures (100 °C, 150 °C and 200 °C) under 50 atm hydrogen pressure for 1 hour to reabsorb hydrogen.

The phase structure for the as-milled samples, before and after desorption and after rehydrogenation, was determined by a Rigaku MiniFlex X-ray diffractometer with Cu K_α radiation. Before the measurement, a small amount of sample was spread uniformly in the sample holder and wrapped with plastic wrap to prevent oxidation. θ -2 θ scans were carried out over diffraction angles from 20° to 80° with a scanning rate of 2.00° min⁻¹. FTIR spectroscopy analyses were carried out using a Thermo Nicolet. Samples were analysed in attenuated total reflectance (ATR) mode equipped with a Ge crystal. Forty (40) scans were carried out between 800 and 2000 cm⁻¹ with a spectral resolution of 4 cm⁻¹.

Thermogravimetric analysis/differential scanning calorimetry (TGA/DSC) of the dehydrogenation process was carried out on a Mettler Toledo TGA/DSC 1. The sample was loaded into an alumina crucible in the glove box. The crucible was then placed in a sealed glass bottle in order to prevent oxidation during transportation from the glove box to the TGA/DSC apparatus. An empty alumina crucible was used for reference. The samples were heated from room temperature to 300 °C under an argon flow of 30 ml•min⁻¹, and different heating rates were used.

3. RESULTS AND DISCUSSION

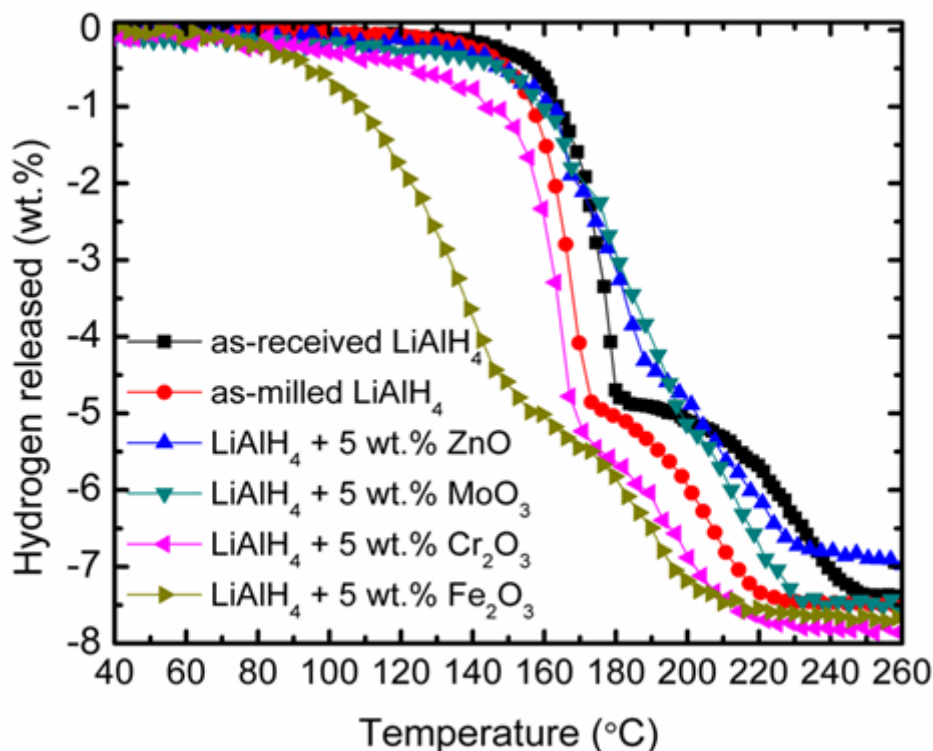


Figure 1. Temperature-programmed desorption patterns for dehydrogenation of as-received LiAlH_4 , as-milled LiAlH_4 , and LiAlH_4 doped with 5 wt.% of ZnO , MoO_3 , Cr_2O_3 , and Fe_2O_3

Figure 1 exhibits the temperature-programmed desorption (TPD) performances of the as-received LiAlH_4 , the as-milled LiAlH_4 , and the LiAlH_4 doped with 5 wt.% of ZnO , MoO_3 , Cr_2O_3 and Fe_2O_3 . The as-received LiAlH_4 started to release hydrogen at about 150 °C in the first step, R_1 ($3\text{LiAlH}_4 \rightarrow \text{Li}_3\text{AlH}_6 + 2\text{Al} + 3\text{H}_2$, where 5.3 wt.% H_2 was theoretically released), and desorbed about 4.99 wt.% hydrogen. The second step reaction, R_2 ($\text{Li}_3\text{AlH}_6 \rightarrow 3\text{LiH} + \text{Al} + 3/2\text{H}_2$, where 2.6 wt.% H_2 was theoretically released), started to release hydrogen at 189 °C and desorbed about 2.53 wt.% hydrogen. The as-milled LiAlH_4 started to release hydrogen at 145 °C for the first stage and desorbed about 4.85 wt.% hydrogen. In the second stage, it started to decompose at 173 °C, and about 2.62 wt.% hydrogen was released. The total amount of hydrogen released from the as-milled LiAlH_4 was about 7.47 wt.%. After milling, compared with the as-received LiAlH_4 , the onset desorption temperatures both slightly decreased by around 5 °C for the first two dehydrogenation steps, indicating that the milling process also influenced the onset desorption temperature of LiAlH_4 due to the activation introduced during mechanical milling [21,32,46]. Among the transition metal oxides used in this study, Fe_2O_3 exhibited a strong catalytic influence on the onset desorption temperature of LiAlH_4 . The Fe_2O_3 -doped LiAlH_4 composite sample started to release hydrogen at about 80 °C and at about 145 °C in the first and second stages, respectively, which represented respective reductions of about 65 °C and about 28 °C compared with as-milled LiAlH_4 . The amounts of hydrogen released were 4.5 and 3.1 wt.% in the first and second stages, respectively. After being doped with Cr_2O_3 , the onset desorption

temperature of LiAlH_4 was slightly decreased. The sample started to release hydrogen at about $120\text{ }^\circ\text{C}$ in the first stage and initiated at about $170\text{ }^\circ\text{C}$ in the second stage and released about 7.9 wt.% hydrogen. It was evident that the addition of Cr_2O_3 exhibited a small beneficial effect on the desorption temperature. This result is in accordance with that reported by Rafi-ud-din et al. [45]. From the results, it was also found that apart from Fe_2O_3 and Cr_2O_3 , the two other transition metal oxide additives, MoO_3 and ZnO , yielded no significant change in both the first and second dehydrogenation stages of the LiAlH_4 .

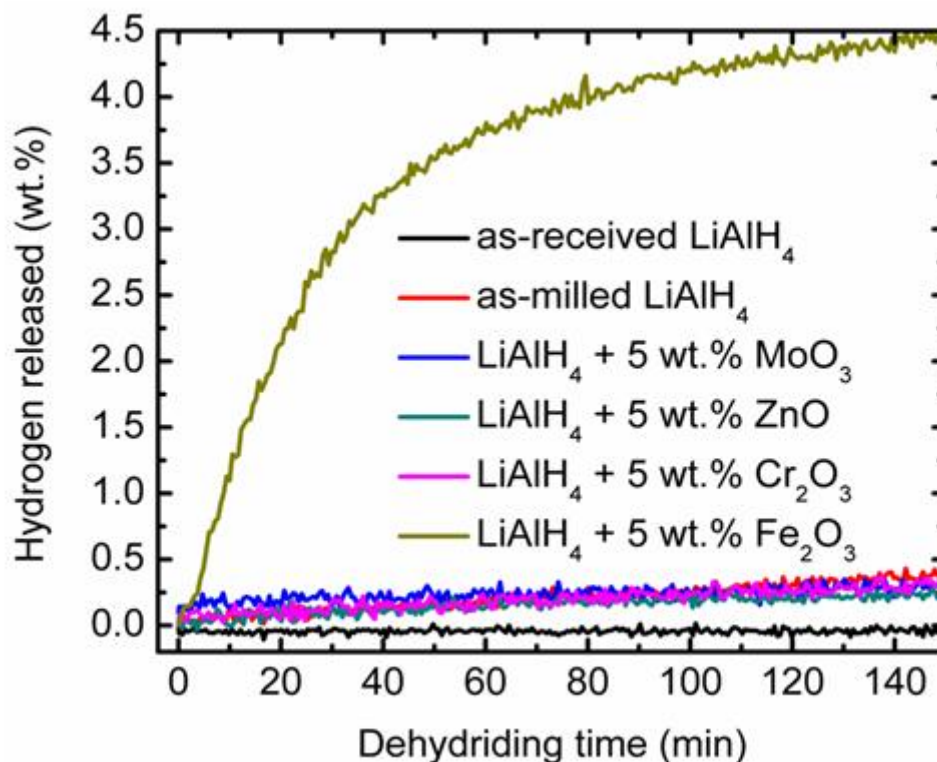


Figure 2. Isothermal desorption kinetics curves for as-received LiAlH_4 , as-milled LiAlH_4 , and $\text{LiAlH}_4 + 5\text{ wt.}\%$ of ZnO , MoO_3 , Cr_2O_3 , and Fe_2O_3 at a constant temperature of $90\text{ }^\circ\text{C}$

Figure 2 shows the results of isothermal dehydrating kinetics measurements for the as-received LiAlH_4 , as-milled LiAlH_4 , and $\text{LiAlH}_4 + 5\text{ wt.}\%$ of ZnO , MoO_3 , Cr_2O_3 , and Fe_2O_3 at a constant temperature of $90\text{ }^\circ\text{C}$, which is considered a comfortable temperature for fuel cell operations. Almost no hydrogen was desorbed at this temperature from the as-received LiAlH_4 . The results show that an addition of Fe_2O_3 gave a significant improvement. The Fe_2O_3 -added sample released about 4.0 wt.% hydrogen after 75 minutes of dehydrogenation, but the as-milled LiAlH_4 and the other transition metal oxide-doped LiAlH_4 samples released less than 0.25 wt.% hydrogen within the same period. The capacity of hydrogen released in this study is slightly lower than those reported by Zhai et al. [46], in which their isothermal dehydrating kinetics result shows that the Fe_2O_3 -doped LiAlH_4 sample could release about 4.7 wt % hydrogen in 70 min at $90\text{ }^\circ\text{C}$. The results show that Fe_2O_3 can be considered as the best metal oxide additive for LiAlH_4 in terms of the onset dehydrogenation temperature, isothermal

desorption kinetics and hydrogen yield, thus leading to an analysis of the Fe_2O_3 mechanism and the catalytic effect in the subsequent test. Although Li et al. [47] has explored the effect of Fe_2O_3 nanoparticles on the dehydrogenation properties of LiAlH_4 , but this study may give the difference in the way Fe_2O_3 take effect and therefore gain a deeper understanding of the modification of dehydrogenation process of LiAlH_4 . This study may be giving an important supplement for the LiAlH_4 -catalyst system.

Figure 3 shows the SEM images of the as-received and as-milled LiAlH_4 and the $\text{LiAlH}_4 + 5$ wt.% Fe_2O_3 . As can be seen, the SEM images of the as-received LiAlH_4 powders (Figure 3a) were shown as irregular rods, and their particle size was between 10-50 μm . However, the as-milled LiAlH_4 and the Fe_2O_3 -doped sample consisted of regular globular particle features, and the particle sizes were not evenly distributed.

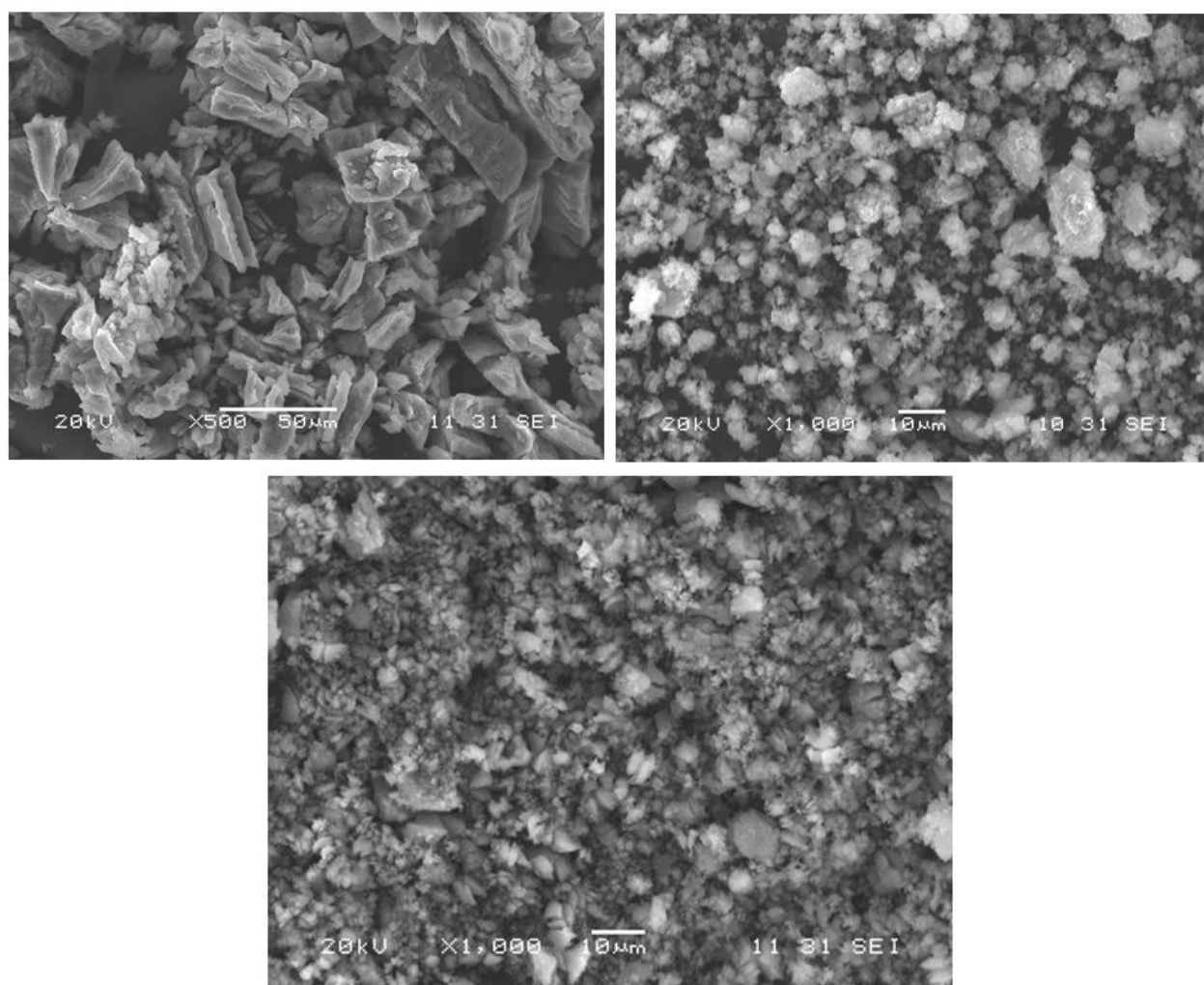


Figure 3. SEM micrographs of (a) as-received LiAlH_4 , (b) as-milled LiAlH_4 and (c) LiAlH_4 doped with 10 wt.% Fe_2O_3 after ball milling

The particle size was between 1-15 μm , as shown in Figure 3b and 3c. Our added Fe_2O_3 particles were < 50 nm of the original size and it was difficult to observe the embedded Fe_2O_3 in the

LiAlH₄ matrix from the SEM images due to extremely small size of Fe₂O₃ particle. From the SEM results, the dehydriding performances of the as-milled LiAlH₄ sample slightly improved attributed to the decrease of the grain size of LiAlH₄ by mechanical milling. Moreover, for the Fe₂O₃-doped LiAlH₄ sample, a high density of nano-sized catalyst particles formed a large amount of nucleation sites at the surface of the LiAlH₄ matrix, and the interface mobility of the transformed phase could conduct along the two-dimensional network of grain boundaries, which all led to the surface activation and larger surface area of the LiAlH₄ particles [46].

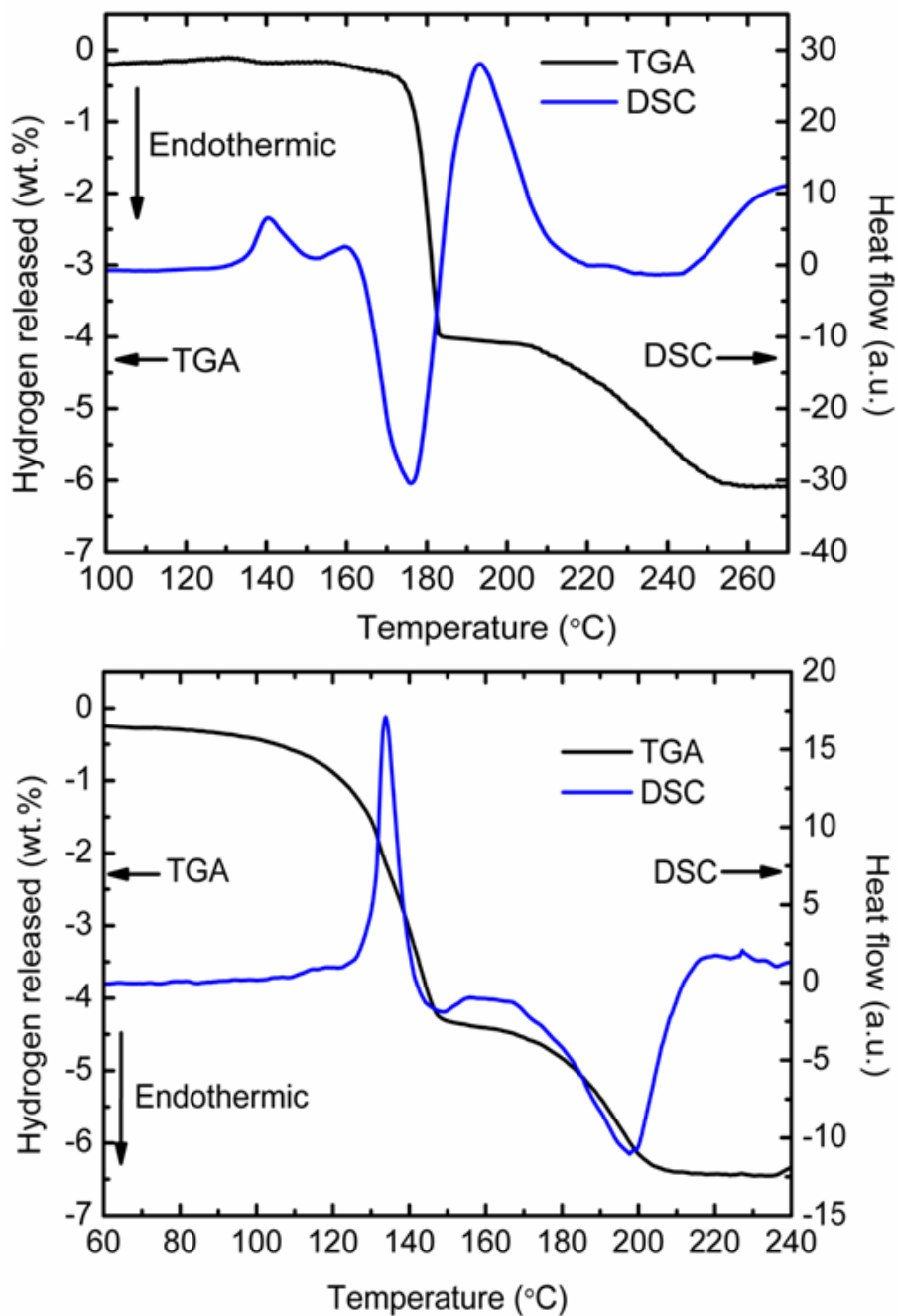


Figure 4. DSC traces of (a) as-received LiAlH₄ and (b) LiAlH₄ + 5 wt.% Fe₂O₃ (Heating rate: 15 °C min⁻¹, argon flow: 30 ml/min)

In order to further analyse the thermal decomposition performances of LiAlH_4 with and without a catalyst, Figures 4a-b illustrate the TGA/DSC results on the as-received LiAlH_4 and the $\text{LiAlH}_4 + 5$ wt.% Fe_2O_3 within the temperature range of 35- 300 °C at heating rates of $10\text{ °C}\cdot\text{min}^{-1}$. For the TGA result, the two major weight loss events in the TGA curve agreed well with the two major stages of dehydrogenation shown by the TPD curve in Figure 1. Meanwhile, for the DSC result, it is clear that for the as-received LiAlH_4 , there were two peaks corresponding to the exothermic processes and two peaks corresponding to the endothermic processes. The first exothermic peak at 160 °C can be assigned to the interaction of the LiAlH_4 with surface hydroxyl impurities, as reported in our previous papers [27,39,42,44,52], and the first endothermic peak at 177 °C corresponded to the melting of the LiAlH_4 [53]. The second exothermic peak at 193 °C corresponded to the decomposition of liquid LiAlH_4 (first reaction stage), and the second endothermic peak at 245 °C was assigned to the decomposition of Li_3AlH_6 (second reaction stage) [54]. For $\text{LiAlH}_4 + 5$ wt.% Fe_2O_3 , the number of thermal events reduced from four to only two. These two thermal events occurred firstly at 120 °C to 145 °C, with an exothermic peak at 132 °C, and then at 170 °C to 220 °C, with an endothermic peak at 198 °C. The exothermic peak at 132 °C for $\text{LiAlH}_4 + 5$ wt.% Fe_2O_3 corresponded to the decomposition of the LiAlH_4 .

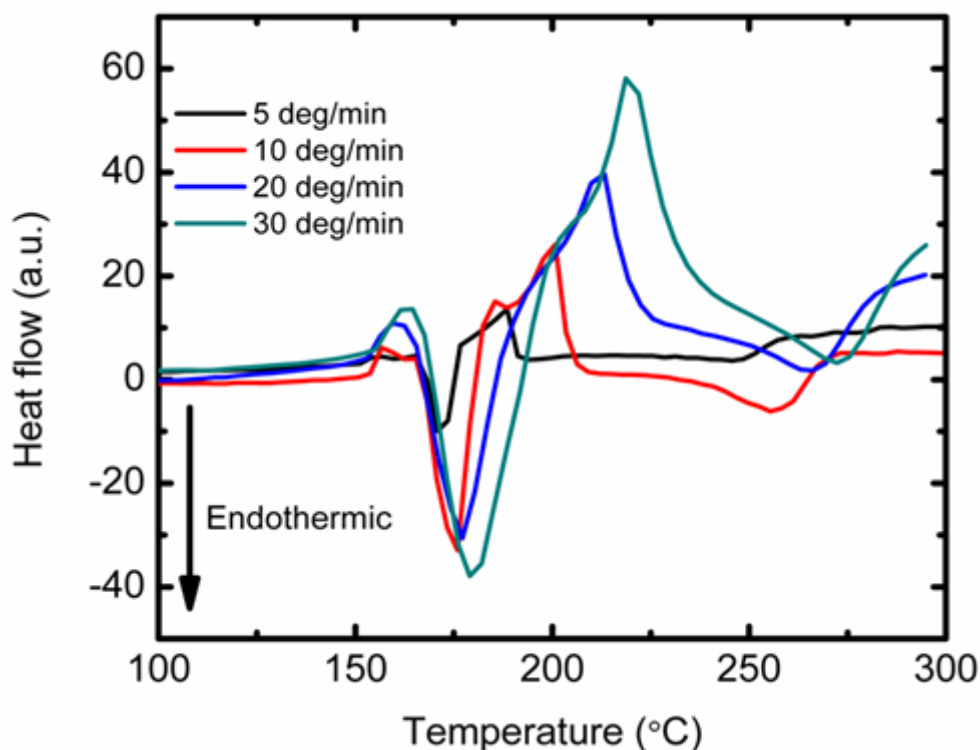


Figure 5. DSC traces at different heating rates for as-received LiAlH_4

This temperature was reduced by 61 °C compared with the temperature observed for the as-received LiAlH_4 . The endothermic peak at 198 °C corresponded to the decomposition of the Li_3AlH_6 , and this temperature was reduced by 47 °C compared to the as-received sample. The first endothermic

effects corresponding to the melting of the LiAlH_4 disappeared from the DSC curve of the Fe_2O_3 -doped material. The disappearance of the melting peak from the DSC trace should be attributed to the fact that the decomposition temperature in the first stage was lower than the melting temperature of the LiAlH_4 . From the DSC results, it can be seen that the onset desorption temperature was quite high compared to the Sievert-type PCT result (Figure 1). This difference is because, in the Sievert-type PCT measurements, the sample was heated in a 0.1 atm vacuum, but in the DSC measurement, the sample was heated under 1 atm argon. Therefore, there is a difference in terms of the driving force of the desorption process. The considerable difference in the dehydrogenating temperature under large and small driving forces indicates that the diffusion of the hydrogen atoms is the rate limiting process in the dehydrogenating reaction, which is in contradiction to what has been reported for the MgNiAlMH system [55].

Rehydrogenation tests were conducted for LiAlH_4 with 5 wt.% added Fe_2O_3 to investigate the reversibility of the Fe_2O_3 -added LiAlH_4 . After the first complete dehydrogenation (first two stages of the reaction), the samples were kept at different temperatures (100 °C, 150 °C and 200 °C) under 50 atm hydrogen pressure for 1 hour to reabsorb hydrogen. From the PCT and XRD results, the rehydrogenation process showed no hydrogen absorption at any temperature. The failure of the rehydrogenation in this system was probably due to the extremely low formation enthalpy of LiAlH_4 and Li_3AlH_6 [34,46]. Theoretically, for a complex hydride to absorb and desorb hydrogen reversibly under practical pressures and temperatures, the hydrogen desorption must be endothermic [56]. From the DSC results, it is clear that for LiAlH_4 , the first reaction stage is exothermic and the second reaction stage is endothermic. Therefore, the first stage reaction is not likely to be reversible, while the second stage reaction is potentially reversible.

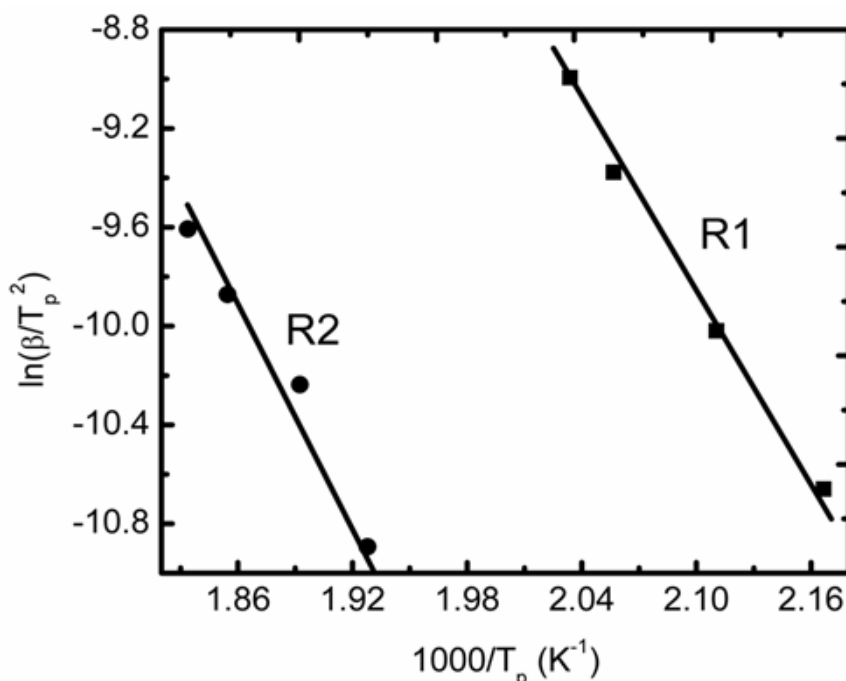


Figure 6. Kissinger plot for first two dehydrogenation stages of as-received LiAlH_4

The enhancement of the dehydrogenation properties of LiAlH_4 after doping with Fe_2O_3 is related to the energy barriers for H_2 release. So, in order to investigate the kinetics enhancement of the $\text{LiAlH}_4\text{-Fe}_2\text{O}_3$ composite in more detail, we used the DSC curves at different heating rates to calculate the activation energy for the first two dehydrogenation steps. Figure 5 shows the DSC traces for the as-received LiAlH_4 at different heating rates (5, 10, 20 and 30 $^\circ\text{C}\cdot\text{min}^{-1}$, respectively). The activation energy, E_A , for the hydrogen desorption was obtained by performing a Kissinger analysis [57], according to the following equation:

$$\ln[\beta/T_p^2] = -E_A/RT_p + A \quad (3)$$

where β is the heating rate, T_p is the peak temperature in the DSC curve, R is the gas constant, and A is a linear constant. Thus, the activation energy, E_A , can be obtained from the slope in a plot of $\ln[\beta/T_p^2]$ versus $1000/T_p$. The E_A values of the as-received LiAlH_4 calculated from the Kissinger analysis (Figure 6) for the first two dehydrogenation steps were 102 and 110 kJ/mol, respectively. Using the same method, the E_A of the Fe_2O_3 -doped sample for the first two dehydrogenation steps were calculated to be 84 and 96 kJ/mol, respectively. From the results, it is clear that the apparent activation energy, E_A , for the two dehydrogenation steps of LiAlH_4 was lowered after the addition of 5 wt.% Fe_2O_3 . From the results, the onset dehydrogenation temperature and the reduction of activation energy, E_A of the Fe_2O_3 -doped LiAlH_4 in this study slightly higher compared to those reported by Li et al. [47]. This difference may due to the different rotate speed of the milling process, as Li et al. reported that the sample was ball milled using high-energy ball mill at the rate of 1200 rpm, as compared to rate of 400 rpm in this study. It is well known that the mean particle size of powder is gradually become small with increasing the rotate speed [58]. Compared to this study, the dehydriding performances of the Fe_2O_3 -doped LiAlH_4 sample reported by Li et al. [47] obtained a drastic advance after ball milling due to the smallest in particle size and crystallite size which resulted in introducing a high surface defect density and creating more grain boundaries.

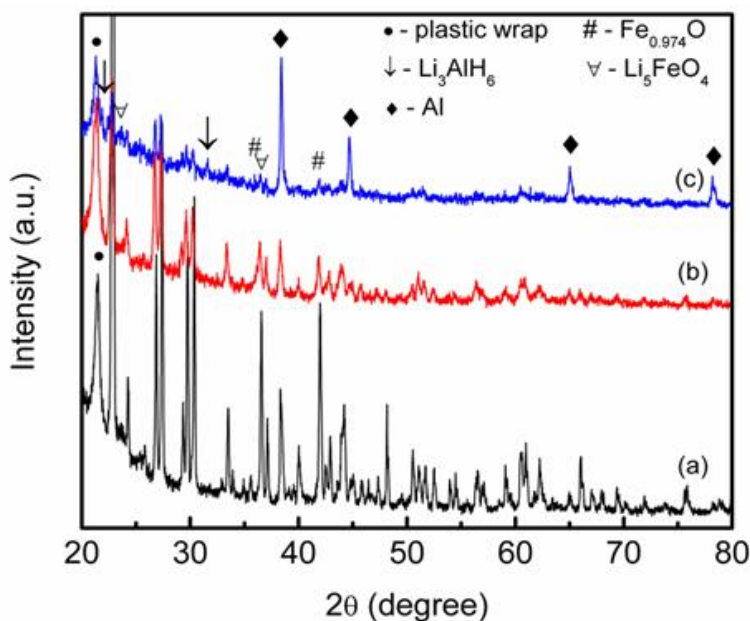


Figure 7. X-ray diffraction patterns of (a) as-received LiAlH_4 , (b) as-milled LiAlH_4 , and (c) LiAlH_4 doped with 5 wt.% Fe_2O_3 after ball milling

In order to determine the phase structures of the sample with or without Fe_2O_3 after ball milling, Figure 7 shows the XRD pattern of the as-milled and as-received LiAlH_4 and the 5 wt.% Fe_2O_3 -doped sample. For the as-received LiAlH_4 , except for the plastic wrap peak, the spectra show that the LiAlH_4 crystallised in the monoclinic space group P21/c. The result is in good agreement with the crystal structure of LiAlH_4 reported by Hauback et al. [59]. The 1-hour ball-milled LiAlH_4 showed slightly weaker intensity compared to the as-received sample, and no additional peaks were observed, indicating the rather high stability of lithium aluminium hydride during mechanochemical treatment. Balema et al. [24] reported that after ball milling for 35 hours, their LiAlH_4 sample showed only weak additional peaks of microcrystalline aluminium, confirming the rather high stability of LiAlH_4 . However, weak additional peaks of Al and Li_3AlH_6 appeared in the XRD spectrum of the Fe_2O_3 - added LiAlH_4 after ball milling. In addition, new peaks corresponding to Li_5FeO_4 and $\text{Fe}_{0.974}\text{O}$ were observed for the doped sample as presented in Figure 7. This result demonstrated that the reaction between LiAlH_4 and Fe_2O_3 occurred during ball milling by forming ternary Li-Fe oxide and Fe oxide species with a reduced valance state. Li et al. [47] reported a similar decomposition reaction occurs between LiAlH_4 and Fe_2O_3 , in which the reaction can take place by forming a ternary $\text{Li}_2\text{Fe}_{2.4}\text{O}_{4.6}$ and $\text{Fe}_{0.957}\text{O}$ species during the ball-milling process. In this study, the forming of Li_5FeO_4 instead of $\text{Li}_2\text{Fe}_{2.4}\text{O}_{4.6}$ as a reaction product may due to different rotate speed of the milling process.

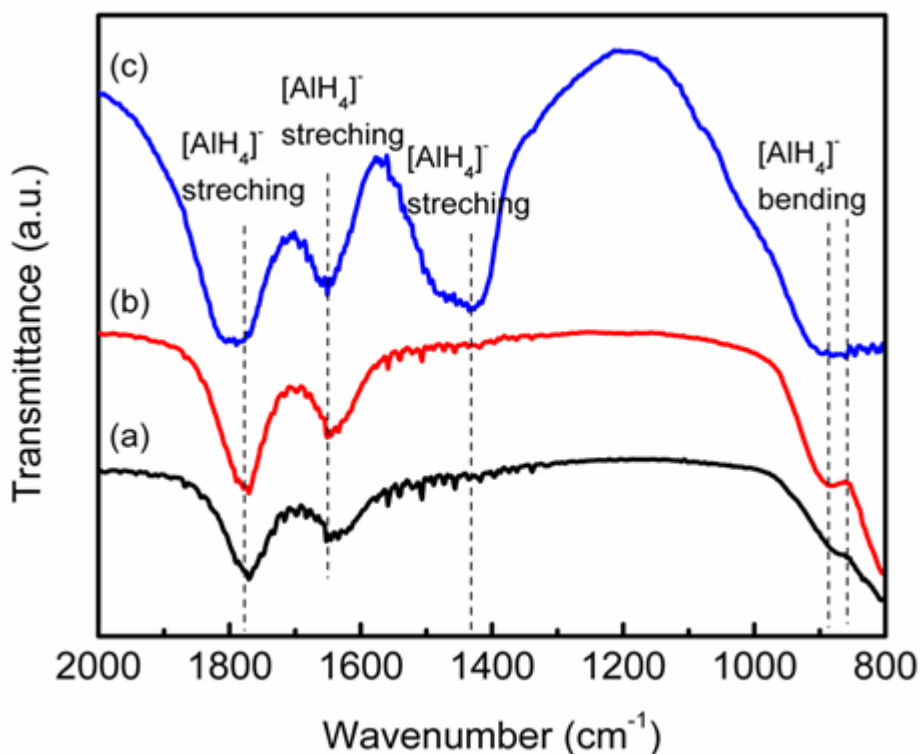


Figure 8. FTIR spectra of (a) as-received LiAlH_4 , (b) as-milled LiAlH_4 , and (c) $\text{LiAlH}_4 + 5$ wt.% Fe_2O_3

The FTIR spectra for the as-received and as-milled LiAlH_4 and Fe_2O_3 -doped LiAlH_4 are compared in Figure 8. For the pristine LiAlH_4 , there were two regions of active infrared vibrations of

the Al-H bonds [28]: two $[\text{AlH}_4]^-$ stretching modes between 1600 and 1800 cm^{-1} , and two $[\text{AlH}_4]^-$ bending modes between 800 and 900 cm^{-1} . From the spectra shown in Figure 8, all the stretching and bending modes occurred for all samples, and they are in good agreement with results previously reported [28]. After doping with Fe_2O_3 , the new peak, at 1425.15 cm^{-1} , appeared. This could be ascribed to the Al-H stretching mode of Li_3AlH_6 [32]. This result confirms that the LiAlH_4 decomposed into Li_3AlH_6 in Fe_2O_3 -doped LiAlH_4 during ball milling; agreeing well with the XRD result (Figure 7).

In order to verify the phase structures of the doped LiAlH_4 sample in the dehydrogenation processes, XRD scans were performed on the 5 wt.% Fe_2O_3 added LiAlH_4 sample after dehydrogenation at 250 °C, as shown in Figure 9. The asreceived LiAlH_4 were also included for comparison purposes. As expected, for the asreceived LiAlH_4 , the spectra show that the dehydrogenated sample at 250 °C consisted of Al and LiH as the dehydrogenation products, with no phases of LiAlH_4 and Li_3AlH_6 . This result indicates that the first and second reactions were completed for LiAlH_4 . However, for the Fe_2O_3 -doped sample, their XRD spectra show that there were not only Al and LiH but also Li_5FeO_4 and $\text{Fe}_{0.974}\text{O}$ as the dehydrogenated products.

A possible mechanism for the Fe_2O_3 effect in the dehydrogenation properties of LiAlH_4 is that during the milling, Fe_2O_3 reacts with LiAlH_4 by forming a ternary Li-Fe oxide and Fe oxide species with a reduced valance state as proved in the present study by the XRD result (Figure 7). These products could act as a real catalyst because they could create surface activation and form a large amount of nucleation sites at the surface of the LiAlH_4 matrix. It is also speculated that these finely dispersed ball-milled products may serve as the active sites for nucleation by shortening the diffusion distance of the reaction ions.

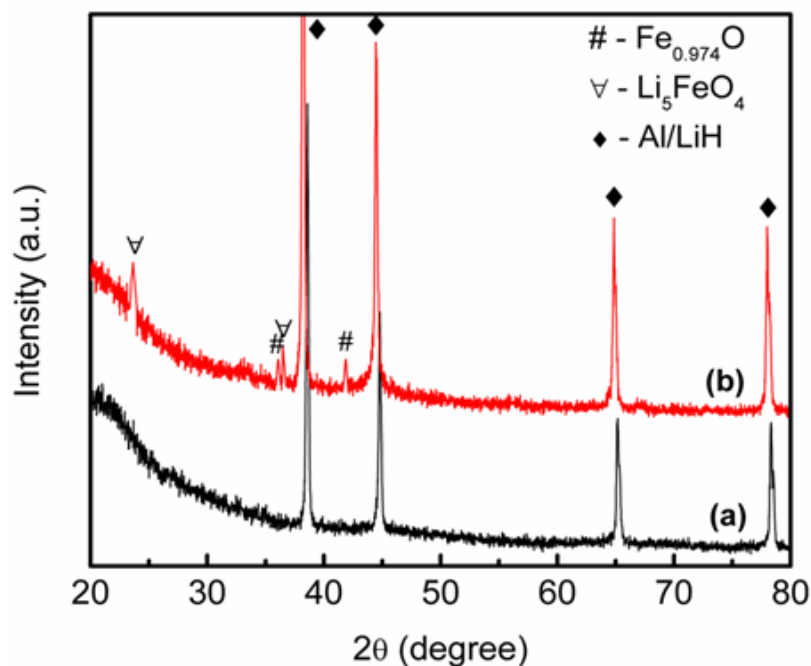


Figure 9. X-ray diffraction patterns for dehydrogenation samples of (a) as-milled LiAlH_4 and (b) $\text{LiAlH}_4 + 5 \text{ wt.}\% \text{Fe}_2\text{O}_3$

Therefore, it is believed that the significant improvement that was observed in the dehydrogenation temperature and kinetics desorption of the Fe₂O₃-doped LiAlH₄ system was a synergistic catalytic effect between the ternary Li-Fe oxide and the catalytic role of the Fe oxide species with a reduced valance state.

4. CONCLUSIONS

The influence of the catalytic activity of the metal oxide nanopowder series (Fe₂O₃, Cr₂O₃, ZnO and MoO₃) on the hydrogen desorption properties of LiAlH₄ prepared by mechanical milling was investigated. Among the additives examined, the Fe₂O₃ exhibited the best improvement in reducing the dehydrogenation temperature and enhancing the dehydrogenation rate. The decomposition temperature of the 5 wt.% Fe₂O₃-added LiAlH₄ sample was reduced to 80 °C and 145 °C in the first and second stages, respectively, compared with 150 °C and 180 °C for the as-received LiAlH₄. In terms of the desorption kinetics, the 5 wt.% Fe₂O₃-added LiAlH₄ sample released about 3.8 wt.% hydrogen at 90 °C after 60 minutes of dehydrogenation, while the as-milled LiAlH₄ and the other metal oxide doped samples released less than 0.3 wt.% hydrogen for the same temperature and duration. From the Kissinger plot, the activation energy for H-desorption from the LiAlH₄ was reduced from 102 and 110 kJ/mol for the first two dehydrogenation steps, to 84 and 96 kJ/mol after the addition of Fe₂O₃. XRD and FTIR analyses for the doped sample showed that LiAlH₄ reacted with Fe₂O₃ during ball milling by forming a ternary Li-Fe oxide and Fe oxide species with a reduced valance state. It is believed that the formation of in-situ Li₅FeO₄ and Fe_{0.974}O together had a synergetic catalytic effect on the dehydrogenation properties of LiAlH₄.

ACKNOWLEDGEMENTS

The author thanks the University Malaysia Terengganu for providing the facilities to carry out this project. The author also acknowledges the Malaysian Government for financial support through the Fundamental Research Grant Scheme (59295).

References

1. L. Schlapbach, A. Züttel, *Nature* 414 (2001) 353-358.
2. V.V. Bhat, C.I. Contescu, N.C. Gallego, F.S. Baker, *Carbon* 48 (2010) 1331-1340.
3. B. Zhou, W. Guo, C. Tang, *Nanotechnology* 19 (2008) 075707.
4. A. Ranjbar, M. Ismail, Z.P. Guo, X.B. Yu, H.K. Liu, *Int. J. Hydrogen Energy* 35 (2010) 7821-7826.
5. J. Mao, Z. Guo, X. Yu, M. Ismail, H. Liu, *Int. J. Hydrogen Energy* 36 (2011) 5369-5374.
6. X.B. Yu, Y.H. Guo, H. Yang, Z. Wu, D.M. Grant, G.S. Walker, *J. Phys. Chem. C* 113 (2009) 5324-5328.
7. X.B. Yu, Y.H. Guo, Z.X. Yang, Z.P. Guo, H.K. Liu, S.X. Dou, *Scripta Mater.* 61 (2009) 469-472.
8. X.B. Yu, Z.X. Yang, H.K. Liu, D.M. Grant, G.S. Walker, *Int. J. Hydrogen Energy* 35 (2010) 6338-6344.
9. N. S. Mustafa, M. Ismail, *Int. J. Hydrogen Energy* 39 (2014) 7834-7841.

10. M. Ismail, *Int. J. Hydrogen Energy* 39 (2014) 2567-2574.
11. Y. Zhang, W.-S. Zhang, M.-Q. Fan, S.-S. Liu, H.-L. Chu, Y.-H. Zhang, X.-Y. Gao, L.-X. Sun, *J. Phys. Chem. C* 112 (2008) 4005-4010.
12. M.A. Wahab, Y. Jia, D. Yang, H. Zhao, X. Yao, *J. Mater. Chem. A* 1 (2013) 3471-3478.
13. X.B. Yu, D.M. Grant, G.S. Walker, *J. Phys. Chem. C* 112 (2008) 11059-11062.
14. X.B. Yu, Z. Wu, Q.R. Chen, Z.L. Li, B.C. Weng, T.S. Huang, *Appl. Phys. Lett.* 90 (2007) 034106.
15. Y. Zhang, Q. Tian, J. Zhang, S.-S. Liu, L.-X. Sun, *J. Phys. Chem. C* 113 (2009) 18424-18430.
16. M. Ismail, *Int. J. Hydrogen Energy* <http://dx.doi.org/10.1016/j.ijhydene.2014.03.166>.
17. B. Bogdanovic, K. Bohmhammel, B. Christ, A. Reiser, K. Schlichte, R. Vehlen, U. Wolf, *J. Alloys Compd.* 282 (1999) 84-92.
18. A. Andreasen, T. Vegge, A.S. Pedersen, *J. Solid State Chem.* 178 (2005) 3672-3678.
19. M. Resan, M.D. Hampton, J.K. Lomness, D.K. Slattey, *Int. J. Hydrogen Energy* 30 (2005) 1413-1416.
20. R.A. Varin, L. Zbronic, T. Czujko, Z.S. Wronski, *Int. J. Hydrogen Energy* 36 (2011) 1167-1176.
21. R.A. Varin, L. Zbronic, *J. Alloys Compd.* 506 (2010) 928-939.
22. V.P. Balema, J.W. Wiench, K.W. Dennis, M. Pruski, V.K. Pecharsky, *J. Alloys Compd.* 329 (2001) 108-114.
23. J. Chen, N. Kuriyama, Q. Xu, H.T. Takeshita, T. Sakai, *J. Phys. Chem. B* 105 (2001) 11214-11220.
24. V.P. Balema, V.K. Pecharsky, K.W. Dennis, *J. Alloys Compd.* 313 (2000) 69-74.
25. R.A. Varin, R. Parviz, *Int. J. Hydrogen Energy* 37 (2012) 9088-9102.
26. K. Hoang, A. Janotti, C.G. Van de Walle, *Phys. Chem. Chem. Phys.* 14 (2012) 2840-2848.
27. M. Ismail, Y. Zhao, X.B. Yu, S.X. Dou, *Int. J. Hydrogen Energy* 35 (2010) 2361-2367.
28. J.R. Ares Fernandez, F. Aguey-Zinsou, M. Elsaesser, X.Z. Ma, M. Dornheim, T. Klassen, R. Bormann, *Int. J. Hydrogen Energy* 32 (2007) 1033-1040.
29. Y. Suttisawat, P. Rangsunvigit, B. Kitiyanan, N. Muangsin, S. Kulprathipanja, *Int. J. Hydrogen Energy* 32 (2007) 1277-1285.
30. X. Zheng, X. Qu, I.S. Humail, P. Li, G. Wang, *Int. J. Hydrogen Energy* 32 (2007) 1141-1144.
31. T. Sun, C.K. Huang, H. Wang, L.X. Sun, M. Zhu, *Int. J. Hydrogen Energy* 33 (2008) 6216-6221.
32. S.-S. Liu, L.-X. Sun, Y. Zhang, F. Xu, J. Zhang, H.-L. Chu, M.-Q. Fan, T. Zhang, X.-Y. Song, J.P. Grolier, *Int. J. Hydrogen Energy* 34 (2009) 8079-8085.
33. R.A. Varin, L. Zbronic, *J. Alloys Compd.* 509, Supplement 2 (2011) S736-S739.
34. Z. Li, S. Liu, X. Si, J. Zhang, C. Jiao, S. Wang, S. Liu, Y.-J. Zou, L. Sun, F. Xu, *Int. J. Hydrogen Energy* 37 (2012) 3261-3267.
35. X. Liu, S.D. Beattie, H.W. Langmi, G.S. McGrady, C.M. Jensen, *Int. J. Hydrogen Energy* 37 (2012) 10215-10221.
36. J. Fu, L. Rontzsch, T. Schmidt, M. Tegel, T. Weibgarber, B. Kieback, *Int. J. Hydrogen Energy* 37 (2012) 13387-13392.
37. J.L. Wohlwend, P.B. Amama, P.J. Shamberger, V. Varshney, A.K. Roy, T.S. Fisher, *J. Phys. Chem. C* 116 (2012) 22327-22335.
38. P.B. Amama, J.T. Grant, P.J. Shamberger, A.A. Voevodin, T.S. Fisher, *J. Phys. Chem. C* 116 (2012) 21886-21894.
39. M. Ismail, Y. Zhao, X.B. Yu, A. Ranjbar, S.X. Dou, *Int. J. Hydrogen Energy* 36 (2011) 3593-3599.
40. L. Hima Kumar, B. Viswanathan, S. Srinivasa Murthy, *Int. J. Hydrogen Energy* 33 (2008) 366-373.
41. Rafi-ud-din, L. Zhang, L. Ping, Q. Xuanhui, *J. Alloys Compd.* 508 (2010) 119-128.
42. M. Ismail, Y. Zhao, X.B. Yu, S.X. Dou, *Int. J. Electroactive Mater.* 1 (2013) 13-22.
43. M.S. Leo Hudson, H. Raghubanshi, D. Pukazhselvan, O.N. Srivastava, *Int. J. Hydrogen Energy* 35 (2010) 2083-2090.
44. M. Ismail, Y. Zhao, X.B. Yu, I.P. Nevirkovets, S.X. Dou, *Int. J. Hydrogen Energy* 36 (2011) 8327-8334.

45. Rafi-ud-din, Q. Xuanhui, L. Ping, L. Zhang, M. Ahmad, *J. Phys. Chem. C* 115 (2011) 13088-13099.
46. F. Zhai, P. Li, A. Sun, S. Wu, Q. Wan, W. Zhang, Y. Li, L. Cui, X. Qu, *J. Phys. Chem. C* 116 (2012) 11939-11945.
47. Z. Li, P. Li, Q. Wan, F. Zhai, Z. Liu, K. Zhao, L. Wang, S. Lu, L. Zou, X. Qu, A.A. Volinsky, *J. Phys. Chem. C* 117 (2013) 18343-18352.
48. Y.T. Wang, C.B. Wan, X.H. Meng, C.Y. Yan, X. Ju, *Int. J. Hydrogen Energy* 38 (2013) 16080-16089.
49. L. Li, C. An, Y. Wang, Y. Xu, F. Qiu, Y. Wang, L. Jiao, H. Yuan, *Int. J. Hydrogen Energy* 39 (2014) 4414-4420.
50. P. Li, Z. Li, F. Zhai, Q. Wan, X. Li, X. Qu, A.A. Volinsky, *J. Phys. Chem. C* 117 (2013) 25917-25925.
51. Z. Li, F. Zhai, Q. Wan, Z. Liu, J. Shan, P. Li, A.A. Volinsky, X. Qu, *RSC Advances* 4 (2014) 18989-18997.
52. M. Ismail, Y. Zhao, X.B. Yu, S.X. Dou, *RSC Advances* 1 (2011) 408-414.
53. M. McCarty, J.N. Maycock, V.R.P. Verneker, *J. Phys. Chem.* 72 (1968) 4009-4014.
54. J.A. Dilts, E.C. Ashby, *Inorg. Chem.* 11 (1972) 1230-1236.
55. T. Spassov, V. Rangelova, P. Solsona, M.D. Baró, D. Zander, U. Köster, *J. Alloys Compd.* 398 (2005) 139-144.
56. S. Satyapal, J. Petrovic, C. Read, G. Thomas, G. Ordaz, *Catal. Today* 120 (2007) 246-256.
57. H.E. Kissinger, *Anal. Chem.* 29 (1957) 1702-1706.
58. J. Song, F. Wang, X. Li, L. Zhao, W. Li, H. Huang, M. Su, *2nd International Conference on Materials, Mechatronics and Automation, Lecture Notes in Information Technology* 15 (2012).
59. B.C. Hauback, H.W. Brinks, H. Fjellvåg, *J. Alloys Compd.* 346 (2002) 184-189.